Approaching Intraband Relaxation Rates in the High-Speed Modulation of Semiconductor Lasers

Weng W. Chow, G. Allen Vawter, *Senior Member, IEEE*, and Junpeng Guo

***Abstract*—This paper uses a nonequilibrium semiconductor laser model to investigate high-modulation bandwidth operation in semiconductor lasers. In particular, limitations to $\gtrsim$ 100 GHz modulation response, which approaches the carrier–phonon scattering rate, are analyzed. It is found that plasma heating leads to a dynamic carrier population bottleneck, which limits scaling of modulation bandwidth. An optical injection scheme is proposed to verify this phenomenon experimentally.**

***Index Terms*—Hot carriers, laser theory, nonequilibrium laser dynamics, optical modulation, quantum-well lasers, semiconductor lasers.**

I. Introduction

ULTRAWIDE-BANDWIDTH optical data link technology continues to be driven by the needs of proposed distributed communication and computing networks. High-capacity data pipelines may well employ multiple wavelength channels comprising of high-speed data at rates approaching or exceeding 100 Gb/s. Direct generation of optical data at such rates remains an interesting possibility, as the capability of high-speed drive electronics continues to improve.

A semiconductor laser is an essential component for optical data generation and transmission. Three factors determine modulation response in semiconductor lasers: 1) electrical parasitics; 2) carrier transport; and 3) carrier relaxation and radiative recombination. The first two factors depend strongly on device engineering, and significant progress made in drive electronics and heterostructure design has resulted in modulation bandwidths in the low tens of gigahertz range [1], [2]. Further improvement (e.g., to the high tens of gigahertz) can conceivably result in modulation speeds that are less than an order of magnitude slower than intraband scattering rates. In that case, factor 3), which involves intrinsic carrier properties in the active medium, can become a limiting factor.

This paper describes an analysis of the physical phenomena within a semiconductor active medium governing high-speed modulation of the laser output. Nonequilibrium carrier dynamics is expected to be important, which eliminates the use of rate equation models [3]. Instead, we use a laser model that is developed for parametric studies of nonequilibrium effects in laser diodes. [4] Extrinsic effects such as parasitics in the drive electronics and carrier transport across a separate confinement heterostructure are not included in the study. On the other hand, intrinsic limitations to high-speed operation, such as those arising from spectral hole burning, plasma heating, carrier capture and thermionic emission are treated at a microscopic level. This is accomplished by working with momentum or k-resolved carrier distributions and polarizations, whose dynamics are described by the semiconductor-Bloch equations [5]. Collisions are treated with the effective relaxation rate approximation, and many-body Coulomb effects are included at the level of the screened Hartree–Fock approximation. While there are more rigorous treatments of nonequilibrium effects involving quantum kinetic approaches [6]–[8], they lead to numerical models that are too computationally intensive to be suitable for parametric studies. However, these treatments based on microscopically determined scattering rates serve the important purpose of justifying the present model.

Details of the laser model are described in Section II. Section III discusses the scaling of modulation bandwidth via increasing excitation or mode-confinement factor. In both cases, the modulation bandwidth eventually saturates because of a dynamical population bottleneck between barrier and quantum-well states. We illustrate this by direct modulation of the laser output with a external optical field.

II. Laser Model

In our laser model, the coupled laser field and semiconductor medium are described by the Maxwell–semiconductor–Bloch equations, [5] which consist of the reduced wave equation for the laser field (in MKS units)

$$\frac{d\mathcal{E}(t)}{dt} = -\gamma_c \mathcal{E}(t) + \frac{i\omega\Gamma}{\varepsilon_b V_{qw}} \sum_{\mathbf{k}_\perp} (\mu_{\mathbf{k}_\perp})^* \, p_{\mathbf{k}_\perp}(t) \tag{1}$$

and the semiconductor–Bloch–equations for the gain medium

$$\frac{dp_{\mathbf{k}_\perp}(t)}{dt} = -i\,(\omega_{\mathbf{k}_\perp} - \omega)\, p_{\mathbf{k}_\perp}(t) - i\Omega_{\mathbf{k}_\perp}(t) \cdot [n^{qw}_{e,\mathbf{k}_\perp}(t) + n^{qw}_{h,\mathbf{k}_\perp}(t) - 1] + \left.\frac{\partial p_{\mathbf{k}_\perp}(t)}{\partial t}\right|_{col} \tag{2}$$

$$\frac{dn^{qw}_{\alpha,\mathbf{k}_\perp}(t)}{dt} = \sum_j [i p_{\mathbf{k}_\perp}(t)^* \Omega_{\mathbf{k}_\perp}(t) + c.c.] - \gamma_{qw} n^{qw}_{\alpha,\mathbf{k}_\perp} + \left.\frac{\partial n^{qw}_{\alpha,\mathbf{k}_\perp}(t)}{\partial t}\right|_{col} \tag{3}$$

$$\frac{dn^{b}_{\alpha,\mathbf{k}}(t)}{dt} = \Lambda_{\alpha,\mathbf{k}}(t) - \gamma_b n^{b}_{\alpha,\mathbf{k}} + \left.\frac{\partial n^{b}_{\alpha,\mathbf{k}}(t)}{\partial t}\right|_{col} \tag{4}$$

Manuscript received November 24, 2003; revised April 8, 2004. This work was supported by the U.S. Department of Energy through Contract DE-AC04–94AL8500.

The authors are with the Sandia National Laboratories, Albuquerque, NM 87185-0601 USA (e-mail: wwchow@sandia.gov).

Digital Object Identifier 10.1109/JQE.2004.831627

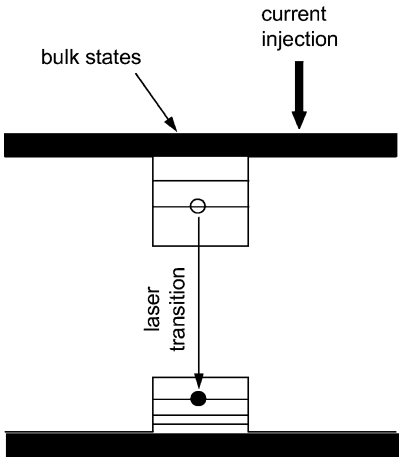

Fig. 1. Quantum-well gain structure with quantum-well (2-D) and barrier (3-D) states for electrons and holes.

where $\alpha = e$ (for electrons) and h (for holes). In (1), $\mathcal{E}(t)$ is a slowly varying complex electric field amplitude, γ_c is the cavity linewidth, ε_b is the background permittivity, Γ is the optical mode-confinement factor, $\mu_{\mathbf{k}_\perp}$ is the dipole matrix element, and V_{qw} is the active region volume. Equations (2) – (4) describe the active medium, which consists of quantum-well [two-dimensional (2-D)] and barrier [three-dimensional (3-D)] states, as sketched in Fig. 1. For the quantum-well equations, (2) – (3), $p_{\mathbf{k}_\perp}$ is the microscopic polarization amplitude, $n^{qw}_{\alpha,\mathbf{k}_\perp}$ is the electron or hole population, and $\mathbf{k}_\perp$ is the in-plane (2-D) momentum. In these equations, the transition and Rabi frequencies, $\omega_{\mathbf{k}_\perp}$ and $\Omega_{\mathbf{k}_\perp}$, respectively, are given by

$$\hbar\omega_{\mathbf{k}_\perp} = \hbar\omega_{\mathbf{k}_\perp,0} + \sum_{\mathbf{q}_\perp\neq\mathbf{0}} V_{\mathbf{q}_\perp}\left(\frac{1}{\varepsilon_{\mathbf{q}_\perp}} - 1\right) - \sum_{\mathbf{k}'_\perp\neq\mathbf{k}_\perp} V_{s,\mathbf{k}_\perp-\mathbf{k}'_\perp}\left(n^{qw}_{e,\mathbf{k}'_\perp} + n^{qw}_{h,\mathbf{k}'_\perp}\right) \quad (5)$$

$$\hbar\Omega_{\mathbf{k}_\perp}(t) = \frac{1}{2}\mu_{\mathbf{k}_\perp}\mathcal{E}(t) + \sum_{\mathbf{k}'_\perp\neq\mathbf{k}_\perp} V_{s,|\mathbf{k}_\perp-\mathbf{k}'_\perp|} p_{\mathbf{k}'_\perp}(t) \quad (6)$$

where $\hbar\omega_{\mathbf{k}_\perp,0}$ is the single-particle transition energy. The many-body contributions in (5) and (6) are the terms containing the screened Coulomb potential in Fourier space $V_{s,\mathbf{q}} = V_{\mathbf{q}_\perp}/\varepsilon_{\mathbf{q}_\perp}$, where $V_{\mathbf{q}_\perp}$ is the 2-D bare (unscreened) Coulomb potential, and $\varepsilon_{\mathbf{q}_\perp}$ is the dielectric function obtained using the static plasmon-pole approximation. [5] For the barrier (4), $n^b_{\alpha,\mathbf{k}}$ is the barrier carrier population, $\mathbf{k}$ is the 3-D momentum, and

$$\Lambda_{\alpha,\mathbf{k}}(t) = \frac{J(t)}{eV_bN_{p,\alpha}} f^b_{\alpha,\mathbf{k}}\left(\mu^l_{p,\alpha}, T_l\right)\left(1 - n^b_{\alpha,\mathbf{k}}\right) \quad (7)$$

is the pump contribution, where J is the injected current density, e is the electron charge, $f^b_{\alpha,\mathbf{k}}$ and $N_{p,\alpha}$ are the steady-state electron or hole distribution and density in the absence of a laser field, and the quantity $(1 - n^b_{\alpha,\mathbf{k}})$ accounts for pump blocking due to the exclusion principle [9]. Nonradiative carrier losses in the quantum-well and barrier regions are described by the terms in (3) and (4) containing the effective carrier decay rates γ_{qw} and γ_b.

The distinctly different timescales for carrier–carrier and carrier–phonon collisions make possible the use of the relaxation rate approximation to write [4]

$$\left.\frac{\partial p_{\mathbf{k}_\perp}}{\partial t}\right|_{col} = -\gamma p_{\mathbf{k}_\perp}(t) \quad (8)$$

$$\left.\frac{\partial n^{qw}_{\alpha,\mathbf{k}_\perp}}{\partial t}\right|_{col} = -\gamma_{c-c}\left[n^{qw}_{\alpha,\mathbf{k}_\perp} - f^{qw}_{\alpha,\mathbf{k}_\perp}\left(\mu^p_\alpha, T_p\right)\right] - \gamma_{c-p}\left[n^{qw}_{\alpha,\mathbf{k}_\perp} - f^{qw}_{\alpha,\mathbf{k}_\perp}\left(\mu^l_\alpha, T_l\right)\right] \quad (9)$$

$$\left.\frac{\partial n^b_{\alpha,\mathbf{k}}}{\partial t}\right|_{col} = -\gamma_{c-c}\left[n^b_{\alpha,\mathbf{k}} - f^b_{\alpha,\mathbf{k}}\left(\mu^p_\alpha, T_p\right)\right] - \gamma_{c-p}\left[n^b_{\alpha,\mathbf{k}} - f^b_{\alpha,\mathbf{k}}\left(\mu^l_\alpha, T_l\right)\right] \quad (10)$$

where γ is the effective polarization dephasing rate, γ_{c-c} is effective carrier–carrier collision rate, and γ_{c-p} is the effective carrier–phonon collision rate. Typical values at room temperature are $\gamma \approx \gamma_{c-c} \simeq 1$ to $2\times10^{13}\ s^{-1}$, and $\gamma_{c-p} \simeq 0.2\times10^{12}\ s^{-1}$ to $10^{12}\ s^{-1}$. Equation (9) models the relaxation, via carrier–carrier and carrier–phonon collisions, of a quantum-well carrier distribution $n^{qw}_{\alpha,\mathbf{k}_\perp}$ to Fermi–Dirac functions $f^{qw}_{\alpha,\mathbf{k}_\perp}$ at chemical potentials and temperatures (μ^p_α, T_p) and (μ^l_α, T_l). Similarly, (10) models the same processes for the bulk distributions. The chemical potentials μ^p_e and μ^p_h, as well as the plasma temperature T_p, are determined by the conservation of total electron or hole density N_α, and conservation of total electron and hole energy ε in carrier–carrier collisions, i.e.,

$$N_\alpha = \frac{n_{qw}}{A}\sum_{\mathbf{k}_\perp} n^{qw}_{\alpha,\mathbf{k}_\perp} + \frac{h_b}{V_b}\sum_{\mathbf{k}} n^b_{\alpha,\mathbf{k}} = \frac{n_{qw}}{A}\sum_{\mathbf{k}_\perp} f^{qw}_{\alpha,\mathbf{k}_\perp}\left(\mu^p_\alpha, T_p\right) + \frac{h_b}{V_b}\sum_{\mathbf{k}} f^b_{\alpha,\mathbf{k}}\left(\mu^p_\alpha, T_p\right) \quad (11)$$

$$\varepsilon = \frac{n_q}{A}\sum_{\alpha,\mathbf{k}_\perp} \varepsilon^{qw}_{\alpha,\mathbf{k}_\perp} n^{qw}_{\alpha,\mathbf{k}_\perp} + \frac{h_b}{V}\sum_{\alpha,\mathbf{k}} \varepsilon^b_{\alpha,\mathbf{k}} n^b_{\alpha,\mathbf{k}} = \frac{n_q}{A}\sum_{\alpha,\mathbf{k}_\perp} \varepsilon^{qw}_{\alpha,\mathbf{k}_\perp} f^{qw}_{\alpha,\mathbf{k}_\perp}(\mu^p_\alpha, T_p) + \frac{h_b}{V}\sum_{\alpha,\mathbf{k}} \varepsilon^b_{\alpha,\mathbf{k}} f^b_{\alpha,\mathbf{k}}(\mu^p_\alpha, T_p) \quad (12)$$

where $\varepsilon^{qw}_{\alpha,\mathbf{k}_\perp}$ and $\varepsilon^b_{\alpha,\mathbf{k}}$ are the single-particle quantum-well and bulk energies, respectively, and h_b is the thickness of the barrier region. To determine the quasi-equilibrium distributions $f^{qw}_{\alpha,\mathbf{k}_\perp}(\mu^l_\alpha, T_l)$ and $f^b_{\alpha,\mathbf{k}}(\mu^l_\alpha, T_l)$ reached by carrier–phonon collisions, we note that while energy is dissipated from the carriers to the crystal lattice by the creation of phonons, the total carrier density is conserved, so that

$$N_\alpha = \frac{n_{qw}}{A}\sum_{\mathbf{k}_\perp} n^{qw}_{\alpha,\mathbf{k}_\perp} + \frac{h_b}{V_b}\sum_{\mathbf{k}} n^b_{\alpha,\mathbf{k}} = \frac{n_{qw}}{A}\sum_{\mathbf{k}_\perp} f^{qw}_{\alpha,\mathbf{k}_\perp}\left(\mu^l_\alpha, T_l\right) + \frac{h_b}{V_b}\sum_{\mathbf{k}} f^b_{\alpha,\mathbf{k}}\left(\mu^l_\alpha, T_l\right). \quad (13)$$

With a common dynamical chemical potential for the barrier and quantum-well quasiequilibrium electron or hole distributions, the exchange of carriers between barrier and quantum-well states, which includes the processes of carrier

capture and escape into and out of, respectively, the quantum well becomes an integral part of the relaxation processes due to carrier–carrier and carrier–phonon collisions.

III. Results

In this paper, we choose as the baseline configuration a laser with a planar microcavity and a gain region consisting of 5-nm-wide $In_{0.75}Ga_{0.25}As$–InP quantum wells. The optical cavity length and facet reflectivities are 50 μm and 0.85, respectively, which give an optical resonator linewidth of $\gamma_c = 10^{12}\ s^{-1}$. The necessity to maximize quantum-well number and cavity linewidth (loss) for high-speed performance is well known [10], [11]. We pick five quantum wells as a reasonable number that can be uniformly pumped by current injection. For a five-quantum-well gain region, $\gamma_c = 10^{12}\ s^{-1}$ is chosen to ensure that threshold current densities are $\lesssim 1\ \mathrm{kA/cm^2}$. The InGaAs–InP material system emits in the 1.5-μm wavelength region which is an advantage for optical fiber transmission. [12] A $\vec{k}\cdot\vec{p}$ calculation [13] is used to determine the bandstructure for $In_{0.75}Ga_{0.25}As$–InP. In particular, the electron and hole energy dispersions are need to determine $\hbar\omega_{\mathbf{k}_\perp,0}$, the single-particle transition energy in (5). Because of the high-compressive strain (1.5%), the quantum well has one electron and three relatively high curvature hole subbands. The high-band curvature and small number of subbands result in a low-transparency carrier density and high differential gain, both of which are desirable for high-speed operation. A small-signal gain calculation indicates that the lasing transition is predominately from the $n = 1$ electron and hole subbands.

With the exception of a gain-switched pulse, one rarely encounters stimulated emission rates ($\lesssim 10^{11}\ s^{-1}$) that approach carrier–carrier scattering rates ($\sim 10^{13}\ s^{-1}$). However, the carrier–phonon scattering rate is an order of magnitude smaller. A typical rate for room temperature electron-longitudinal optical (LO) phonon scattering is $\gamma_{c-p} \approx 10^{12}\ s^{-1}$, so that nonequilibrium effects, such as plasma heating, may be present when modulating in the vicinity of 100 GHz. To illustrate this, the modulation response is calculated for different carrier–phonon scattering rates, and a sinusoidally varying injection current

$$J(t) = (1-\delta) + \delta\cos(\Omega t) \tag{14}$$

where δ is chosen so that the modulation depth $\Delta = (I_{\max} - I_{\min})/I_{\max} = 0.8$ at low modulation frequencies. The laser modulation response is defined as the difference between the maximum and minimum laser intensities, $I_{\max}$ and $I_{\min}$, respectively, with the low-frequency response normalized to unity. A heterostructure with an effective waveguide thickness of 0.23 μm is used. This gives a mode-confinement factor $\Gamma = 0.1$, which, in turn, results in a threshold current density of $J_{\mathrm{th}} = 420\ \mathrm{A/cm^2}$. The calculations are performed with the laser operating with current density $J = 10J_{\mathrm{th}}$.

Fig. 2 shows the dependence of modulation response on carrier–phonon scattering rate γ_{c-p}. We assume a carrier–carrier scattering rate of $\gamma_{c-c} = 10^{13}\ s^{-1}$. The different curves indicate relatively weak variations in the relaxation oscillation frequency and modulation bandwidth with changing carrier–phonon scattering rate. In contrast, there is noticeable γ_{c-p} dependence in the damping of the modulation amplitude. In terms of device performance, the difference between the $\gamma_{c-p} = 2\times 10^{11}\ s^{-1}$ and $5\times 10^{11}\ s^{-1}$ curves is significant. Noting that at room temperature, $5\times 10^{11} \lesssim \gamma_{c-p} \lesssim 10^{12}\ s^{-1}$, the discrepancy between rate equation (dotted curve) and nonequilibrium predictions is appreciable, which justifies the use of the more complicated nonequilibrium laser model.

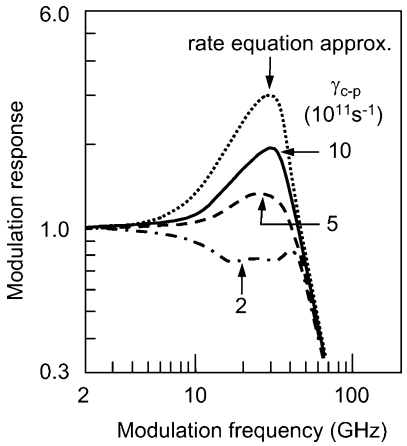

Fig. 2. Modulation response under current modulation for InGaAs–InP quantum-well structure with excitation $J/J_{\mathrm{th}} = 10$. The carrier–phonon scattering rates are $\gamma_{c-p} = 10^{12}$ (solid curve), 5×10^{11} (dashed curve), and $2\times 10^{11}\ s^{-1}$ (dot-dashed curve). The dotted curve is the rate equation result.

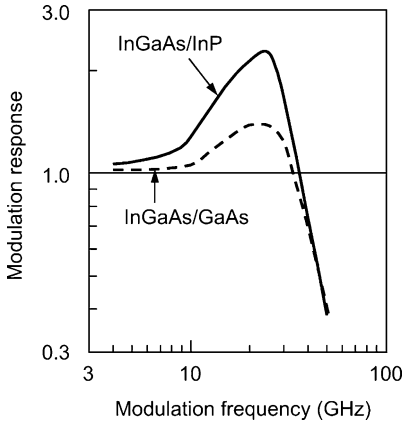

Fig. 3. Modulation response under current modulation for InGaAs–InP (solid curve) and InGaAs–GaAs (dashed curve) quantum-well structures. The carrier–phonon scattering rates are $\gamma_{c-p} = 10^{12}\ s^{-1}$ and excitation is at $J/J_{\mathrm{th}} = 5$.

Another advantage of the present model is that comparison of lasers may be made at the level of bandstructure differences, i.e., in terms of differences in $\omega_{\mathbf{k}_\perp,0}$ and $\mu_{\mathbf{k}_\perp}$ in (5) and (6). For example, the two widely used laser systems, InGaAs–InP and InGaAs–GaAs, have distinctly different conduction and valence band energy dispersions, and optical dipole transition matrix elements. Fig. 3 describes how these bandstructure differences translate to differences in modulation response. In this comparison, we use the same resonator parameters, i.e., $\gamma_c = 10^{12}\ s^{-1}$, $\Gamma = 0.2$. For the InGaAs–GaAs laser, the gain region consist of five 5-nm $In_{0.2}Ga_{0.8}As$–GaAs quantum wells, which has the same 1.5% compressive strain as the InGaAs-InP structure. Due to the high compressive strain, the lowest energy

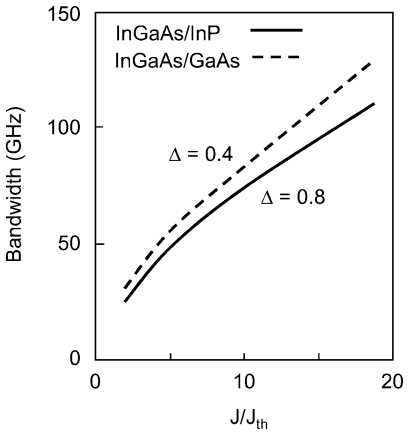

Fig. 4. Modulation bandwidth versus excitation for InGaAs–InP quantum-well structure and modulation depth $\Delta = 0.8$ (solid curve) and 0.4 (dashed curve).

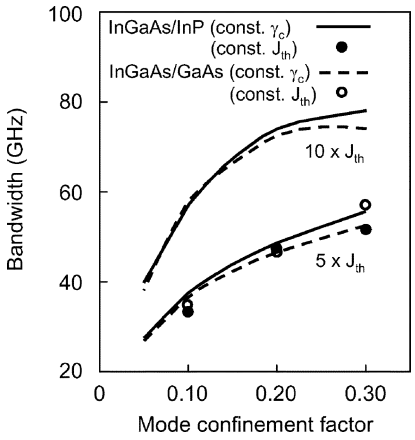

Fig. 5. Modulation bandwidth versus mode-confinement factor for excitation $J/J_{\rm th} = 5$ and 10. The gain structures are InGaAs–InP (solid curve) and InGaAs–GaAs (dashed curve). The circles are obtained assuming equal threshold current densities for both lasers (see Table I).

electron and hole subbands in both lasers are to a good approximation parabolic close to zone center, and therefore, may be described with effective masses. The electron (hole) effective masses are 0.039 m_e (0.050 m_e) for the InGaAs–InP structure and 0.060 m_e (0.102 m_e) for the InGaAs–GaAs structure, where m_e is the free electron mass. From a small-signal gain analysis [5], we found that this roughly factor of 2 difference in effective masses leads to appreciable difference in threshold current density: $J_{\rm th} = 0.37$ kA/cm^2 for InGaAs–InP, compared to 0.79 kA/cm^2 for InGaAs–GaAs. The analysis also indicates a difference in the differential gain: 1.1×10^{-8} cm for InGaAs–InP, compared to 3×10^{-9} cm for InGaAs–GaAs, where the values are taken at the gain peak, and for carrier densities giving a peak gain of 10^3 cm^{-1}.

Fig. 3 plots the modulation response for modulation depth of $\Delta = 0.8$ for both lasers, operating at ten times above their respective lasing thresholds. The curves indicate that the differences in modulation response occur mostly in the modulation amplitudes, especially in the neighborhood of the relaxation oscillation frequencies. Interestingly, the -3-dB modulation bandwidths are similar. This insensitivity of the bandwidth to active medium structure is also observed in experiment, and has been attributed to the cancellation of competing effects [11]. That is also the case in our results, with the higher differential gain $\partial G/\partial N$ in InGaAs–InP balanced by the higher threshold current density $J_{\rm th}$ in InGaAs–GaAs, as is clearly displayed in the well-known expression for the relaxation oscillation frequency [14]. However, it should be noted that this formula is derived assuming a small modulation depth, whereas the results in Fig. 3 are for $\Delta = 0.8$. Furthermore, the modulation bandwidth depends not only on the relaxation oscillation frequency, but also on the modulation amplitude damping.

To explore the scaling to higher modulation bandwidth, we first examine the effects of operating a laser further above its lasing threshold. Fig. 4 plots the modulation bandwidth as a function of excitation for the InGaAs–InP laser. We use a cavity linewidth and confinement factor of $\gamma_c = 10^{12}\ s^{-1}$ and $\Gamma = 0.2$, respectively. The solid curve, which is for a modulation depth $\Delta = 0.8$, indicates a sublinear dependence on $J/J_{\rm th}$. Also, it indicates a theoretical modulation bandwidth of 75 GHz for $J = 10J_{\rm th}$. As expected from the discussion in the previous paragraph, the results for the InGaAs–GaAs laser are similar. However, the calculation assumes equal lattice temperatures for both lasers, which may be unlikely at high excitations, given that $J_{\rm th} = 800$ A/cm^2 for the InGaAs–GaAs laser compared to 400 A/cm^2 for the InGaAs–InP laser. While plasma heating effects are included in the analysis, lattice heating is not. To account for lattice heating effects would require a heat diffusion treatment and detailed knowledge of the heat sinking. Fig. 4 also shows the modulation bandwidth for a modulation depth of $\Delta = 0.4$ (dashed curve). Comparison with the $\Delta = 0.8$ curve shows a degradation of modulation bandwidth with increasing modulation depth. There is also a slight decrease in saturation at the lower modulation depth.

According to earlier investigations, modulation bandwidth may also be increased by increasing the mode-confinement factor. [10], [11] Fig. 5 plots the modulation bandwidth as a function of confinement factor for relative excitations, $J/J_{\rm th} = 5$ and 10. We use optical cladding layer separations ranging from 0.075 and 0.225 μm to obtain mode-confinement factors $0.05 \leq \Gamma \leq 0.30$. The solid and dashed curves are for the InGaAs–InP and InGaAs–GaAs lasers, respectively. Consistent with Fig. 2, there are only minor differences in the modulation bandwidth curves of the two laser systems. For both excitations, there is appreciable improvement in modulation bandwidth at low Γ. However, beyond $\Gamma = 0.2$, the bandwidth saturates, especially at the higher excitation.

Up to this stage, the comparison of material systems is made for lasers with equal cavity linewidth γ_c (corresponding to resonator loss) and relative excitation $J/J_{\rm th}$. In other words, the lasers in the comparison are operated with very different injection currents. An alternative is to use different cavity linewidths, while maintaining the same current density in both lasers. The solid and hollow circles (for InGaAs–InP and InGaAs–GaAs, respectively) in Fig. 5 are for the combinations listed in the first three rows of Table I, with $J = 4$ kA/cm^2 and varying γ_c to maintain $J/J_{\rm th} = 5$. Comparison of the circles and curves

TABLE I
COMBINATIONS OF MODE CONFINEMENT FACTOR, THRESHOLD CURRENT DENSITIES AND CAVITY LINEWIDTHS USED IN THE COMPARISONS OF $In_{0.75}Ga_{0.25}As$-INP AND $In_{0.20}Ga_{0.80}As$-GAAS LASERS

	InGaAs/InP		InGaAs/GaAs	
Γ	$J_{th}(kA/cm^2)$	$\gamma_c\,(10^{12}s^{-1})$	$J_{th}(kA/cm^2)$	$\gamma_c\,(10^{12}s^{-1})$
0.1	0.8	3.3	0.8	0.3
0.2	0.8	6.4	0.8	0.9
0.3	0.8	10	0.8	1.6
0.1	0.42	1	1.00	1
0.2	0.37	1	0.79	1
0.3	0.34	1	0.75	1

indicates only minor differences in the results between fixing the current density or the cavity linewidth (last three rows of Table I).

Overall, the results in Figs. 4 and 5 show that a modulation bandwidth in the 60–80 GHz range is possible before intrinsic limitations due to carrier dynamics become a factor. Of course, the experimental conditions for achieving such a high-modulation speed are quite stringent. A relative excitation of $J/J_{\rm th} = 10$ means injection current densities of $J = 4\,{\rm kA/cm^2}$ for the InGaAs–InP laser and a demanding $J = 8\ {\rm kA/cm^2}$ for the InGaAs–GaAs laser. To achieve a mode-confinement factor of $\Gamma = 0.3$ for a five-quantum-well active region, with each quantum well being 5-nm wide, requires a lateral optical mode width of $< 0.1\ \mu$m. Because of optical diffraction, fabricating the necessary separate confinement heterostucture is challenging. We should also remind ourselves that electrical parasitics and carrier transport are neglected in our analysis. However, there is experimental evidence that experimental devices are approaching the intrinsic limits predicted by our model. An example is the modulation bandwidth of 40 GHz bandwidth reported for an InGaAs–GaAs quantum-well laser. [1] Based on the laser structure described in the paper, we estimate a confinement factor of $\Gamma \approx 0.15$, which places the result relatively close what is predicted in Fig. 5.

To understand the causes of bandwidth saturation in Figs. 4 and 5, we modulate the quantum-well population directly with an external optical field

$$\mathcal{E}_{inj}(t) = \frac{1}{2}\left[\mathcal{E}_0 \sin\left(\frac{\Omega t}{2}\right) e^{-i\omega_i t} + c.c.\right] \tag{15}$$

where ω_i is the applied field frequency and $I_{inj} = \varepsilon_0 c \mathcal{E}_0^2/2$ is its intensity. The injection of optical pulses is a useful technique for studying carrier dynamics in a semiconductor medium [15],

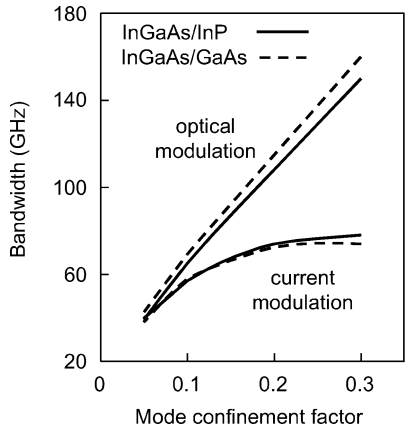

Fig. 6. Modulation bandwidth versus mode-confinement factor for current and optical modulation. The lasers operate at $J/J_{\rm th} = 10$ with InGaAs–InP (solid curve) and InGaAs–GaAs (dashed curve) quantum-well gain structures.

[16]. Additionally, optical injection is being explored as a high-speed switching scheme [17], [18]. The external field changes the quantum-well carrier populations by stimulated emission or absorption, thus modifying (3) according to (16) and (17), shown at the bottom of the page, where we assume side injection to eliminate resonator effects. We have used the rate equation approximation to adiabatically eliminate the polarization dynamics involving the injected optical field. This is valid because the modulation rate of interest is $< 10^{12}$ Hz, which is considerably less than the polarization dephasing rate. In this case, the rate equation approximation can also be used to simplify (2) – (4), without lost of accuracy. Fig. 6 depicts the modulation bandwidths for both optical and current modulation, with cavity linewidth $\gamma_c = 10^{12}\ s^{-1}$ and $J = 10J_{\rm th}$ for both lasers. The curves clearly show the absence of saturation effects, and the feasibility of modulation rates in excess of 100 GHz, when the bulk states are bypassed with optical modulation. This result suggests a dynamical population bottleneck as the primary cause of bandwidth saturation in current modulated lasers. This bottleneck appears as a delayed and attenuated response of the quantum-well carrier population to an applied modulation of the bulk carrier population [4]. The limitation depends on the carrier capture rate which in present case is limited by the carrier–phonon relaxation rate. The InGaAs–InP (solid) and InGaAs–GaAs (dashed) curves indicate that the effect is basically independent of material system. It is, however, relatively sensitive to the carrier–phonon scattering rate as shown in Fig. 7. Notice that the figure depicts a modulation bandwidth that increases with decreasing γ_{c-p}, which is contrary to intuition. An explanation is only possible when taking into account nonequilibrium effects. A slower intraband relaxation causes the formation of nonequilibrium carrier population distributions, because

$$\left.\frac{dn^{qw}_{e,\mathbf{k}_\perp}(t)}{dt}\right|_{inj} = -\sum_j \left[\frac{\mu_{\mathbf{k}_\perp}\mathcal{E}_{inj}(t)}{2\hbar}\right]^2 \frac{2\gamma}{\gamma^2 + (\omega_{\mathbf{k}_\perp} - \omega_i)^2}\left[n^{qw}_{e,\mathbf{k}_\perp}(t) + n^{qw}_{h,\mathbf{k}_\perp}(t) - 1\right] \tag{16}$$

$$\left.\frac{dn^{qw}_{h,\mathbf{k}_\perp}(t)}{dt}\right|_{inj} = -\sum_i \left[\frac{\mu_{\mathbf{k}_\perp}\mathcal{E}_{inj}(t)}{2\hbar}\right]^2 \frac{2\gamma}{\gamma^2 + (\omega_{\mathbf{k}_\perp} - \omega_i)^2}\left[n^{qw}_{e,\mathbf{k}_\perp}(t) + n^{qw}_{h,\mathbf{k}_\perp}(t) - 1\right] \tag{17}$$

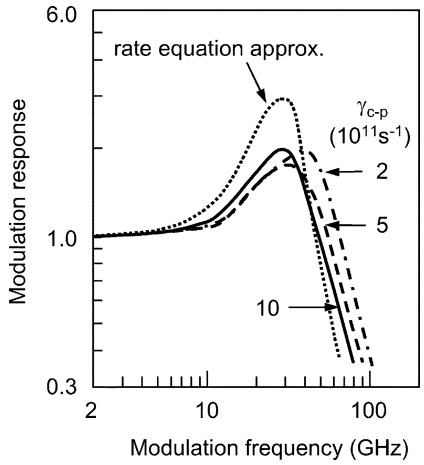

Fig. 7. Modulation response under optical modulation for InGaAs–InP quantum-well structure with excitation $J/J_{\rm th} = 10$. The carrier–phonon scattering rates are $\gamma_{c-p} = 10^{12}$ (solid curve), 5×10^{11} (dashed curve) and $2 \times 10^{11}\ s^{-1}$ (dot-dashed curve). The dotted curve is the rate equation result.

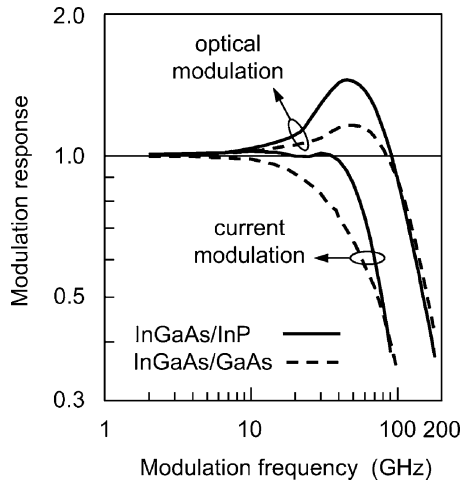

Fig. 8. Modulation response for current and optical modulation and with confinement factor $\Gamma = 0.3$. The lasers operate at $J/J_{\rm th} = 10$ with InGaAs–InP (solid curve) and InGaAs–GaAs (dashed curve) quantum-well gain structures.

the replenishment of quantum-well inversion cannot keep pace with the depletion of gain by the external field. Such a situation is exactly what is desired for a high-speed optical modulation scheme.

Last, we emphasize that lack of changes in modulation bandwidth does not necessarily imply insensitivity in modulation response. Fig. 8 illustrates this by plotting the modulation response of InGaAs–InP (solid curves) and InGaAs–GaAs (dashed curves) for current and optical modulation. The lasers have confinement factor $\Gamma = 0.3$, cavity linewidth $\gamma_c = 10^{12}\ s^{-1}$ and operate with $J = 10J_{\rm th}$. While the modulation bandwidths are basically similar for the two material systems, there is appreciable differences in the modulation responses. In particular, for current modulation, the modulation response degrades at a much lower modulation rate in InGaAs–GaAs than in InGaAs–InP.

IV. Conclusion

We have presented an analysis of semiconductor modulation response at modulation rates comparable to intraband scattering times. Our results indicate that nonequilibrium effects will be important in these high-speed semiconductor lasers. In particular, the dynamic carrier population bottleneck will limit laser modulation bandwidth scaling to high-modulation rates. This paper shows that direct comparison of electrical and optical modulation performance may be used as a tool for understanding the underlying physical limitations.

Acknowledgment

The authors would like to thank C. Sullivan for fruitful discussions.

References

[1] S. Weisser, E. C. Larkins, K. Czotscher, W. Benz, J. Daleiden, I. Esquivias, J. Fleissner, J. D. Ralston, B. Romero, R. E. Sah, A. Schönfelder, and J. Rosenzweig, "Damping-limited modulation bandwidths up to 40 GHz in undoped short-cavity $In_{0.35}Ga_{0.65}As$–GaAs multiple-quantum-well lasers," *IEEE Photon. Technol. Lett.*, vol. 8, pp. 608–610, May 1996.

[2] Y. Matsui, H. Murai, S. Arahira, Y. Ogawa, and A. Suzuki, "Enhanced modulation bandwidth for strain-compensated InGaAsAs–InGaAsP MQW lasers," *IEEE J. Quantum Electron.*, vol. 34, pp. 1970–1975, Oct. 1998.

[3] K. Y. Lau, "Dynamics of quantum-well lasers," in *Quantum Well Lasers*, P. S. Zory Jr., Ed. New York: Academic, 1993, ch. 5.

[4] W. W. Chow, H. C. Schneider, S. W. Koch, C. H. Chang, L. Chrostowski, and C. J. Chang-Hasnain, "Nonequilibrium model for semiconductor laser modulation response," *IEEE J. Quantum Electron.*, vol. 38, pp. 402–409, Apr. 2002.

[5] W. W. Chow and S. W. Koch, *Semiconductor-Laser Fundamentals: Physics of the Gain Materials*. Berlin, Germany: Springer–Verlag, 1999.

[6] F. Jahnke and S. W. Koch, "Theory of carrier heating through injection pumping and lasing in semiconductor microcavity lasers," *Opt. Lett.*, vol. 18, pp. 1438–1440, 1993.

[7] ——, "Ultrafast intensity switching and nonthermal carrier effects in semiconductor microcavity lasers," *Appl. Phys. Lett.*, vol. 67, pp. 2278–2280, 1995.

[8] R. Binder and S. W. Koch, "Non-equilibrium semiconductor dynamics," *Progr. Quantum Electron.*, vol. 19, pp. 307–460, 1995.

[9] S. W. Koch, F. Jahnke, and W. W. Chow, "Physics of semiconductor microcavity lasers," *Semicond. Sci. Technol.*, vol. 10, pp. 739–751, 1995.

[10] J. E. Bowers, B. R. Hemenway, A. H. Gnauck, and D. P. Wilt, "High-speed InGaAsP-constricted-mesa lasers," *IEEE, J. Quantum Electron.*, vol. QE-22, pp. 833–844, June 1986.

[11] J. D. Ralston, S. Weisser, I. Esquivias, E. C. Larkins, J. Rosenzweig, P. Tasker, and J. Fleissner, "Contol of differential gain, nonlinear gain, and damping factor for high-speed application of GaAs-based MQW lasers," *IEEE J. Quantum Electron.*, vol. 29, pp. 1648–1659, June 1993.

[12] C. H. Chang, L. Chrostowski, C. J. Chang-Hasnain, and W. W. Chow, "Study of long-wavelength VCSEL-VCSEL injection locking for 2.5 Gb/s transmission," *Photon. Technol. Lett.*, vol. 14, pp. 1635–1637, Nov. 2002.

[13] G. Bastard, *Wave Mechanics Applied to Semiconductor Heterostructures*. Paris, France: Les Editions de Physique, 1988.

[14] G. P. Agrawal and N. K. Dutta, *Long-Wavelength Semiconductor Lasers*. New York: Van Norstrand Reinhold, 1986.

[15] A. Platonov, C. Lingk, J. Feldmann, M. Arzberger, G. Böhm, M.-C. Amann, and G. Abstreiter, "Ultafast switch-off of an electrically pumped quantum-dot laser," *Appl. Phys. Lett.*, vol. 81, pp. 1177–1179, 2002.

[16] A. Barchanski, T. Gensty, C. Degen, I. Fischer, and W. Elsäßer, "Picosecond emission dynamics of vertical-cavity surface-emitting lasers: Spatial, spectral and polarization-resolved characterization," *IEEE J. Quantum Electron.*, vol. 39, pp. 850–858, July 2003.

[17] H. Uenohara, Y. Kawamura, H. Iwamura, K. Nonaka, H. Tsuda, and T. Kurokawa, "Operation characteristics of a side-light-injection mulitple-quantum-well bistable laser for all-optical switching," *Jpn. J. Appl. Phys.*, vol. 33, pp. 815–821, 1994.

[18] J. L. Fitz, W. T. Beard, S. C. Horst, and S. D. Smith, "Integrated photonic inverter with gain," *IEEE Photon. Technol. Lett.*, vol. 13, pp. 478–480, May 2001.

Weng W. Chow received the Ph.D. degree in physics from the University of Arizona, Tuscon. His dissertation work involved fluctuation phenomena in quantum optics.

He was an Associate Professor of Physics and Astronomy at the University of New Mexico, Albuquerque, before joining Sandia National Laboratories, Albuquerque, where he is currently a Distinguished Member of the Technical Staff. He is also an Adjunct Professor of optical sciences at the University of Arizona and an Honorary Professor of physics at Cardiff University, U.K. His primary research interest is in the application of microscopic theory to semiconductor laser device development. Some of this work is described in two texts, *Semiconductor-Laser Physics* (Berlin, Germany: Springer–Verlag, 1994) and *Semiconductor-Laser Fundamentals: Physics of the Gain Materials* (Berlin, Germany: Springer–Verlag: 1999). His other interests include laser gyros, phased arrays, coupled lasers, quantum optics, and optical ignition of pyrotechnics.

Dr. Chow is a Fellow of the Optical Society of America, and recipient of the Department of Energy, Basic Energy Science/Material Science Award, and the Alexander von Humboldt Forschungspreise.

G. Allen Vawter (S'86–M'87–SM'98) received the Ph. D. degree in electrical engineering from the University of California, Santa Barbara, in 1987. His doctoral thesis involved design and fabrication of photonic integrated circuits, combining etched-facet AlGaAs diode lasers with passive optical routing waveguides for intrachip optical interconnects. He also demonstrated the first etched-facet laser by reactive-ion etching and self-aligned Si and Zn diffusion into AlGaAs.

He is currently a Distinguished Member of Technical Staff working in the Center for Compound Semiconductor Science and Technology at Sandia National Laboratories, Albuquerque, NM. His primary interests include optoelectonic device technology and chemically assisted ion-beam etching of high-performance optoelectronic and photonic structures. Recent activities include all-optical switching in diode-laser logic circuits, silica planar lightwave circuits for WDM and sensor applications, photonic integrated circuits, traveling-wave photodiodes, all-optical generation of millimeter-waves, and novel photonic crystals. He holds 16 patents and has published over 110 papers in recognized technical journals.

Dr. Vawter is a member of Tau Beta Pi.

Junpeng Guo received the Ph.D. degree in electrical engineering from the University of Illinois, Urbana-Champaign, in 1998. His dissertation work involved ultrafast optics, polarization optics, micro/nano optics, and optical holography. He pioneered the work of micropolarizer array for polarization imaging and built the first tunable wavelength ultrafast figure-eight fiber laser.

He joined Rockwell International Science Center, Thousand Oaks, CA, as a Research Scientist, where he worked on various projects involving RF optical signal processing, optical beam steering, and liquid crystal optics. He took a leave from Rockwell to join a high-tech startup company to develop high-speed uncooled semiconductor laser for optical communications. He was responsible for developing the first practical uncooled 10-Gb/s optical transmitter in the industry. Since he joined Sandia National Laboratories in 2002, he has been working on various projects involving nano/micro structure optics, photonic integrated circuits, and ultrafast optics. His primary interest is nano/micro structure optics and ultrafast laser-material/device interactions.